Research Article

Effect of Inclined Magnetic Field on the Entropy Generation in an Annulus Filled with NEPCM Suspension

Seyyed Masoud Seyyedi [iD],[1] **M. Hashemi-Tilehnoee** [iD],[1] **and M. Sharifpur** [iD][2,3,4]

[1]*Department of Mechanical Engineering, Aliabad Katoul Branch, Islamic Azad University, Aliabad Katoul, Iran*
[2]*Department of Mechanical Engineering, University of Science and Culture, Tehran, Iran*
[3]*Department of Mechanical and Aeronautical Engineering, University of Pretoria, Pretoria 0002, South Africa*
[4]*Department of Medical Research, China Medical University Hospital, China Medical University, Taichung, Taiwan*

Correspondence should be addressed to Seyyed Masoud Seyyedi; s.masoud_seyedi@aliabadiau.ac.ir and M. Sharifpur; msharifpur@usc.ac.ir

The encapsulation technique of phase change materials in the nanodimension is an innovative approach to improve the heat transfer capability and solve the issues of corrosion during the melting process. This new type of nanoparticle is suspended in base fluids call NEPCMs, nanoencapsulated phase change materials. The goal of this work is to analyze the impacts of pertinent parameters on the free convection and entropy generation in an elliptical-shaped enclosure filled with NEPCMs by considering the effect of an inclined magnetic field. To reach the goal, the governing equations (energy, momentum, and mass conservation) are solved numerically by CVFEM. Currently, to overcome the low heat transfer problem of phase change material, the NEPCM suspension is used for industrial applications. Validation of results shows that they are acceptable. The results reveal that the values of Nu_{ave} descend with ascending Ha while N_{gen} has a maximum at Ha = 16. Also, the value of $N_{T,MF}$ increases with ascending Ha. The values of Nu_{ave} and N_{gen} depend on nondimensional fusion temperature where good performance is seen in the range of $0.35 < \theta_f < 0.6$. Also, Nu$_{ave}$ increases 19.9% and ECOP increases 28.8% whereas N_{gen} descends 6.9% when ϕ ascends from 0 to 0.06 at $\theta_f = 0.5$. Nu$_{ave}$ decreases 4.95% while N_{gen} increases by 8.65% when Ste increases from 0.2 to 0.7 at $\theta_f = 0.35$.

1. Introduction

Nanofluids can be produced by adding the nanosized particles (such as copper and silver) into the base fluids (i.e., oils, water, and so on). Many researchers scrutinized the effects of conventional nanofluids on fluid flow in different cases [1–14]. Recently, a new type of nanofluids has been constructed using phase change materials (PCMs) which are known as NEPCMs. As we know, PCMs have various applications such as energy-efficient buildings [15], cooling of electronic equipment [16], waste heat recovery [17], ventilation systems [18], and solar energy storage [19]. Although PCMs are used in many industrial applications, the low thermal conductivity of PCMs is a disadvantage for systems with charge and discharge cycles. Some techniques were

proposed to overcome this problem, such as inserting the fins in the PCM enclosure [20, 21], carbon nanotubes in the PCM [22], and using the multilayer PCMs [23, 24]. Furthermore, microencapsulated phase change materials (MPCMs) are used for thermal energy storage [25].

In 2004, the melting process of a PCM was analytically investigated by Hamdan and Al-Hinti [26], where a constant heat flux was imposed on the vertical wall. In 2016, the melting of PCM in a cylindrical medium was studied experimentally and numerically by Azad et al. [27]. In 2017, simulation of melting of a PCM for thermal energy storage was performed by Vikas et al. [28]. They modeled the melting of a rectangular PCM domain using ANSYS (Fluent). In 2017, a simplified model for melting of a PCM in the presence of radiation and natural convection was proposed

by Souayfane et al. [29]. They found that natural convection has an important role during the PCM melting process. In 2018, Selimefendigil et al. [30] studied the free convection of CuO–water nanofluid in an enclosure where a PCM and a conductive partition were attached to its vertical wall by the finite element method. Hosseini et al. [31, 32] studied heat transfer in a horizontal shell-and-tube heat exchanger with a PCM. In 2018, characterizations of natural convection in vertical cylindrical shell-and-tube latent heat thermal energy storage (LHTES) systems were numerically and experimentally investigated by Seddegh et al. [33]. In 2018, Jmal and Baccar [34] studied the PCM solidification numerically where vertical fins were installed in a rectangular module. In 2019, Ghalambaz et al. [35] concluded that fusion temperature defines a dynamic behavior for NECPMs. In a similar work, Hajjar et al. [36] reached to the previous result in analyzing the transient fluid flow in a cavity filled by NEPCM. In 2020, Hasehmi-Tilehnoee et al. [37] studied natural convection and entropy generation in a complex medium filled with nanofluid and NEPCM suspension. They used ANSYS-Fluent to solve the nondimensional form of the governing equations. Different methods have been employed to solve the governing equations such as finite difference method (FDM) [38–40], finite element method (FEM) [41, 42], control volume finite element method (CVFEM) [43–48], and homotopy perturbation method (HPM) [49–51].

In this work, the entropy generation and natural convection are scrutinized in a medium located between concentric horizontal wavy-circular wall and elliptical enclosure filled by NEPCMs suspension.

Preference of this study regarding the earlier studies can be summarized as follows:

(1) A complex porous medium enclosure filled with NEPCM suspension is considered

(2) An inclined magnetic field is applied to the fluid flow

(3) The effects of decision parameters such as Ra, Ha, β, Da, A, N, Ste, θ_f, ϕ, Nc, Nv, and λ (see the Nomenclature) are investigated on heat transfer and entropy generation

(4) The ratio of heat transfer to entropy generation is evaluated

2. Problem Definition

2.1. Physical Model. The porous medium shown in Figure 1 consists of a heated horizontal wavy cylinder at T_h that is concentrically placed inside an elliptic enclosure held at T_c. An external uniform magnetic field $(B_0 = (B_x^2 + B_y^2)^{1/2}$ and $\beta = \tan^{-1}(B_y/B_x))$ has an effect on the fluid flow. The wavy wall of the inner cylinder can be implemented with the following equation:

$$r = r_{\text{in}} + A \cos(N(\zeta - \zeta_0)). \tag{1}$$

2.2. Mathematical Model

2.2.1. Dimensionless Governing Equations. The fluid flow is supposed to be steady, incompressible, two-dimensional, and laminar with no radiation effect. The fluid properties are constant but Boussinesq approximation is applied to the density in the buoyancy term. The dimensionless conservation equations are as follows [14, 35]:

$$\frac{\partial^2 \Psi}{\partial X^2} + \frac{\partial^2 \Psi}{\partial Y^2} = -\Omega,$$

$$\left[\frac{\partial \Psi}{\partial Y}\frac{\partial \Omega}{\partial X} - \frac{\partial \Psi}{\partial X}\frac{\partial \Omega}{\partial Y}\right] = \frac{\mu_b/\mu_f}{\rho_b/\rho_f}\Pr\left(\frac{\partial^2 \Omega}{\partial X^2} + \frac{\partial^2 \Omega}{\partial Y^2}\right) + \frac{\beta_{T,b}}{\beta_{T,f}}\text{Ra}\Pr\frac{\partial \theta}{\partial X} - \frac{\mu_b/\mu_f}{\rho_b/\rho_f}\frac{\Pr}{\text{Da}}\Omega$$

$$+ \frac{\sigma_b/\sigma_f}{\rho_b/\rho_f}\text{Ha}^2\Pr_f\left(\cos^2\beta\frac{\partial^2 \Psi}{\partial X^2} + \sin^2\beta\frac{\partial^2 \Psi}{\partial Y^2} + 2\sin\beta\cos\beta\frac{\partial^2 \Psi}{\partial X\,\partial Y}\right),$$

$$\left[\frac{\partial \Psi}{\partial Y}\frac{\partial \theta}{\partial X} - \frac{\partial \Psi}{\partial X}\frac{\partial \theta}{\partial Y}\right] = \frac{k_b/k_f}{\text{Cr}}\left(\frac{\partial^2 \theta}{\partial X^2} + \frac{\partial^2 \theta}{\partial Y^2}\right),$$

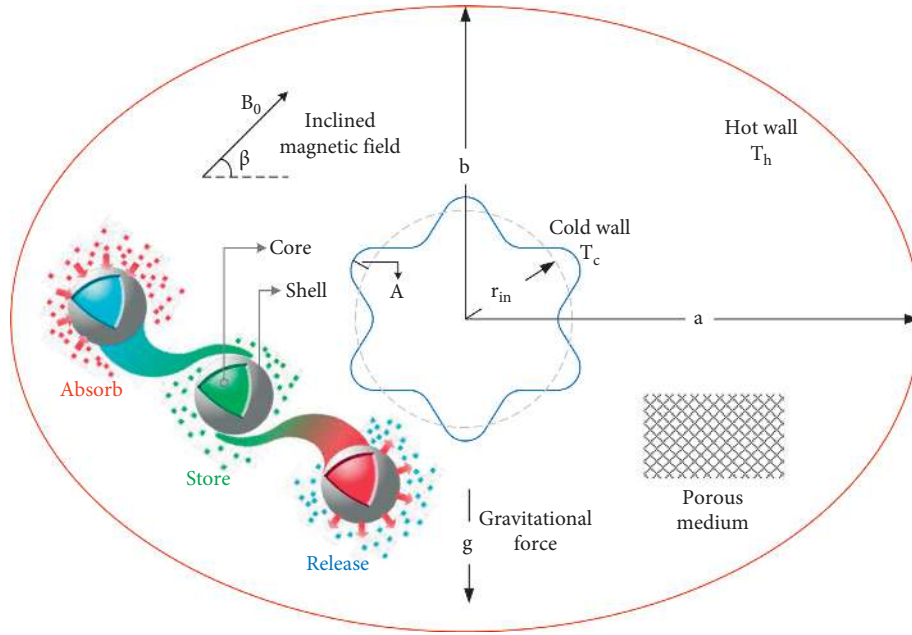$$\tag{2}$$

Figure 1: Schematic view of the considered problem.

where Pr, Ra, Da, Ha, and Cr are given as follows:

$$\text{Ra} = \frac{g\beta_f L^3 (T_h - T_c)}{\nu_f \alpha_f},$$

$$\text{Pr} = \frac{\nu_f}{\alpha_f},$$

$$\text{Ha} = B_0 L \sqrt{\frac{\sigma_f}{\rho_f \nu_f}}, \tag{3}$$

$$\text{Da} = \frac{K}{L^2},$$

$$\text{Cr} = \frac{(\rho C_P)_b}{(\rho C_P)_f},$$

where

$$\frac{k_b}{k_f} = 1 + Nc\phi, \tag{4}$$

$$\frac{\sigma_b}{\sigma_f} = 1 + Ns\phi, \tag{5}$$

$$\frac{\mu_b}{\mu_f} = 1 + Nv\phi. \tag{6}$$

The heat capacity ratio (Cr) can be rewritten in the nondimensional form as follows [35]:

$$\text{Cr} = \frac{(\rho C_P)_b}{(\rho C_P)_f} = (1 - \phi) + \phi\lambda + \frac{\phi}{\delta \text{Ste}} f. \tag{7}$$

Also, f is the nondimensional fusion function defined by the following equation [52]:

$$f = \frac{\pi}{2} \sin\left(\frac{\pi}{\delta}\left(\theta - \theta_f + \frac{\delta}{2}\right)\right) \times \begin{cases} 0, & \theta < \theta_f - \dfrac{\delta}{2}, \\ 1, & \theta_f - \dfrac{\delta}{2} < \theta < \theta_f + \dfrac{\delta}{2}, \\ 0, & \theta_f + \dfrac{\delta}{2} < \theta. \end{cases} \tag{8}$$

The boundary conditions of the system are as follows:

$$\Psi = 0 \text{ and } \theta = 1.0 \text{ on the inner boundary,}$$
$$\Psi = 0 \text{ and } \theta = 0.0 \text{ on the outer boundary.} \tag{9}$$

The average Nusselt number can be calculated using the local Nusselt number along the hot wall as follows:

$$Nu_{\text{local}} = -\left(\frac{k_b}{k_f}\right)\left(\frac{\partial\theta}{\partial r}\right)_{r=R},$$

$$Nu_{\text{ave}} = \frac{1}{2\pi} \int_0^{2\pi} Nu_{\text{local}}(\zeta) d\zeta. \tag{10}$$

2.2.2. Entropy Generation. The performance of energy systems has been evaluated by equation (11) which is named as the rate of entropy generation as follows:

$$\dot{S}_{\text{gen}} = \frac{k_{bf}}{T_0^2}\left[\left(\frac{\partial T}{\partial x}\right)^2 + \left(\frac{\partial T}{\partial y}\right)^2\right]$$

$$+ \frac{\mu_{bf}}{T_0}\left[2\left(\frac{\partial u}{\partial x}\right)^2 + 2\left(\frac{\partial v}{\partial y}\right)^2 + \left(\frac{\partial u}{\partial y} + \frac{\partial v}{\partial x}\right)^2\right] + \frac{\mu_b(u^2 + v^2)}{KT_0} + \frac{\sigma_b B_0^2(u\sin\beta - v\cos\beta)^2}{T_0}. \tag{11}$$

The local entropy generation in nondimensional form can be rewritten as follows [14]:

$$N_{L,\text{gen}} = \frac{\dot{S}_{\text{gen}}}{\left[(k_f/T_0^2)(\Delta T/L)^2\right]} = \underbrace{\frac{k_b}{k_f}\left[\left(\frac{\partial\theta}{\partial X}\right)^2 + \left(\frac{\partial\theta}{\partial Y}\right)^2\right]}_{N_{L,HT}} + \underbrace{\frac{\mu_b}{\mu_f}\Phi_f\left[4\left(\frac{\partial^2\Psi}{\partial X\,\partial Y}\right)^2 + \left(\frac{\partial^2\Psi}{\partial Y^2} - \frac{\partial^2\Psi}{\partial X^2}\right)^2\right]}_{N_{L,FF}}$$

$$+ \underbrace{\frac{1}{\text{Da}}\frac{\mu_b}{\mu_f}\Phi_f\left[\left(\frac{\partial\Psi}{\partial X}\right)^2 + \left(\frac{\partial\Psi}{\partial Y}\right)^2\right]}_{N_{L,PM}} + \underbrace{\frac{\sigma_b}{\sigma_f}\text{Ha}^2\Phi_f\left[\frac{\partial\Psi}{\partial Y}\sin\beta + \frac{\partial\Psi}{\partial X}\cos\beta\right]^2}_{N_{L,MF}}. \tag{12}$$

The total entropy generation and the entropy generation number (N_{gen}) can be obtained, respectively, as follows:

$$N_{T,j} = \int_V N_{L,j}\mathrm{d}V,$$
$$N_{\text{gen}} = \sum_j N_{T,j}, \tag{13}$$

where j denotes the HT, FF, PM, and MF. For more details, see Refs. [13, 14].

Furthermore, the ecological coefficient of performance (ECOP) is calculated by the following [53]:

$$\text{ECOP} = \frac{Nu_{\text{ave}}}{N_{\text{gen}}}. \tag{14}$$

3. Numerical Procedure

A FORTRAN code based on the control volume finite element method (CVFEM) has been extended to solve the governing equations.

3.1. Grid Test. The results of the grid independence study are provided in Table 1. The calculations have been performed with Ra = 10^5, Pr = 6.2, Da = 10^{-2}, ϕ = 0.05, $Nv = Nv = 3$ δ = 0.05, Ste = 0.313, θ_f = 0.3, λ = 0.4, Ha = 30, β = 60°, A = 0.3, N = 6, and Φ = 10^{-4}. Hence, 81×971 can be considered as the grid size.

3.2. Validation. In order to validate the results, two validations are performed. Firstly, the isotherms, streamlines, and Cr contour for a square cavity are obtained for θ_f = 0.5 at Ra = 10^5. Figure 2 shows the results of the present code and those of Ghalambaz et al. [35]. Secondly, the values of average Nusselt number are calculated for several cases that

Table 2 presents the outcomes. Other parameters are constant such as ϕ = 0.05, λ = 0.4, ρ_p/ρ_f = 0.9, and δ = 0.05. For both validations, the results are acceptable.

4. Results and Discussion

In this paper, the second law of thermodynamics and the free convection heat transfer are numerically studied in a medium between concentric horizontal wavy-circular and elliptical cylinders loaded with a dilute suspension by CVFEM. The effects of nondimensional parameters on the characteristics of the flow and entropy generation number are considered. The effect of an external inclined magnetic field on the fluid flow is specified by Hartmann number (Ha) and angle of the magnetic field (β). Darcy number (Da) is used for modeling porous medium. Some decision variables are employed for modeling of NEPCM such as ϕ, λ, δ, Ste, Nv, Nv, Ns, and θ_f. Also, the geometry of enclosure is specified by A and N. The default values of the nondimensional parameters for calculations are presented in Table 3.

Figure 3 shows the isotherms, the streamlines, and Cr contours at Ra = 10^3, 10^4, and 10^5. The power of the flow increases with the Rayleigh number as it is obvious from the maximum value of the absolute stream function, $|\Psi_{\text{max}}|$. The values of $|\Psi_{\text{max}}|$ are 0.44, 3.86, and 16.93 for Ra = 10^3, 10^4, and 10^5, respectively. The isotherms are concentric circles around the hot wall at Ra = 10^3. The convective heat transfer is predominant in this case, while the role of convection in heat transfer becomes more significant with increasing the Rayleigh number. The red lines in isotherms go up from the upper section of the inner wall to the outer wall at Ra = 10^5. The average Nusselt number ascends with ascending the Rayleigh number where the values of Nu_{ave} are 2.5784, 2.9136, and 5.8065, for Ra = 10^3, 10^4, and 10^5, respectively.

The last row in this figure presents the Cr contours for each Rayleigh number. According to equations (7) and (8),

TABLE 1: The effect of grid size on the maximum absolute value of stream function, the average Nusselt number, and the entropy generation number.

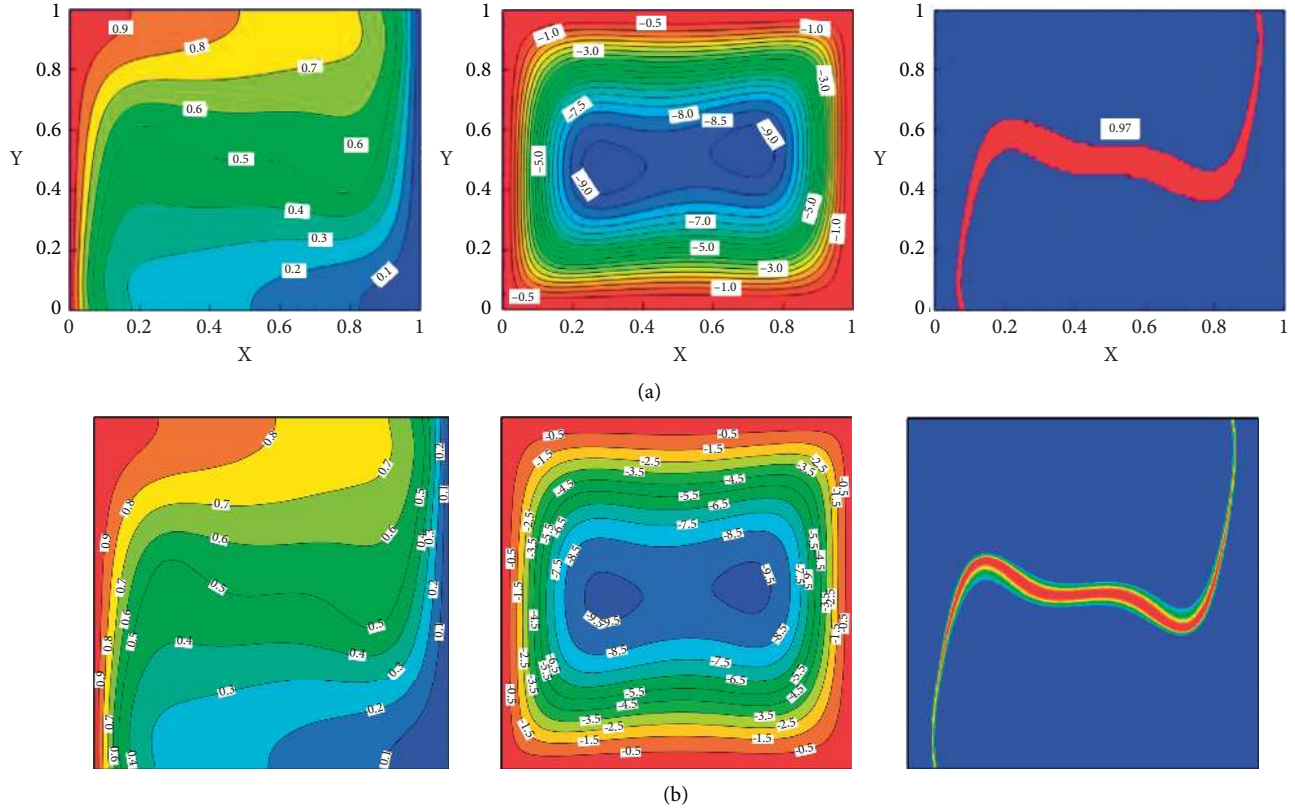|	31×371	41×491	51×611	61×731	71×851	81×971	91×1091
Ψ_{max}	11.50	10.96	10.88	10.34	10.25	10.18	10.16
Nu_{ave}	3.9329	3.8580	3.8012	3.7523	3.7391	3.7345	3.7342
N_{gen}	38.19	37.23	37.02	36.98	36.71	36.69	36.68

(a)

(b)

FIGURE 2: The isotherms, streamlines, and Cr contour at $\theta_f = 0.5$ and Ra = 10^5 for (a) Ghalambaz et al. [35] and (b) present work ($Cr_{max} = 5.988$ and $Cr_{min} = 0.97$).

TABLE 2: The comparison of Nu_{ave} between the Ghalambaz et al. [35] and present work.

No.	θ_f	Ste	N_c	N_v	Nu_{ave}		
					Ghalambaz et al. [35]	Present work	Error (%)
1	0.3	0.313	3	3	5.1932	5.2246	0.6
2	0.3	0.313	6	6	5.4477	5.4705	0.4
3	0.1	0.313	3	3	4.9550	4.9685	0.3
4	0.3	0.2	3	3	5.3541	5.3652	0.2

Cr has a minimum value that is corresponding to $f = 0$ (other parameters are assumed to be constant). For example, for $\phi = 0.05$, $\lambda = 0.4$, $\delta = 0.05$, and Ste = 0.313, the minimum value of Cr is 0.97 (when $f = 0$). Also, Cr has a maximum value that depends on θ_f in the f correlation. Here, the maximum value of Cr is 5.988 (this value can be obtained by solving the velocity and temperature fields). The values of 0.97 and 5.988 are the same for each value of the Rayleigh number in this figure. Notice that the heat capacity changes since the phase change occurs. Other decision

parameters for this figure are Ha = 15, Da = 10, $\theta_f = 0.65$, $\beta = 0°$, and A = 0.1.

Figure 4 presents the effects of the magnetic field and its angle on the entropy generation number and the average Nusselt number. Figure 4(a) shows that Nu_{ave} decreases with ascending Ha while N_{gen} has a maximum at Ha = 16. For instance, Nu_{ave} descends from 5.5496 to 3.6542 (34.15% decreasing) when Ha increases from 0 to 40. Also, N_{gen} increases from 42.60 to 44.06 (3.43% increasing) when Ha increases from 0 to 16 while it decreases from 44.06 to 35.43

TABLE 3: The default values of the nondimensional parameters.

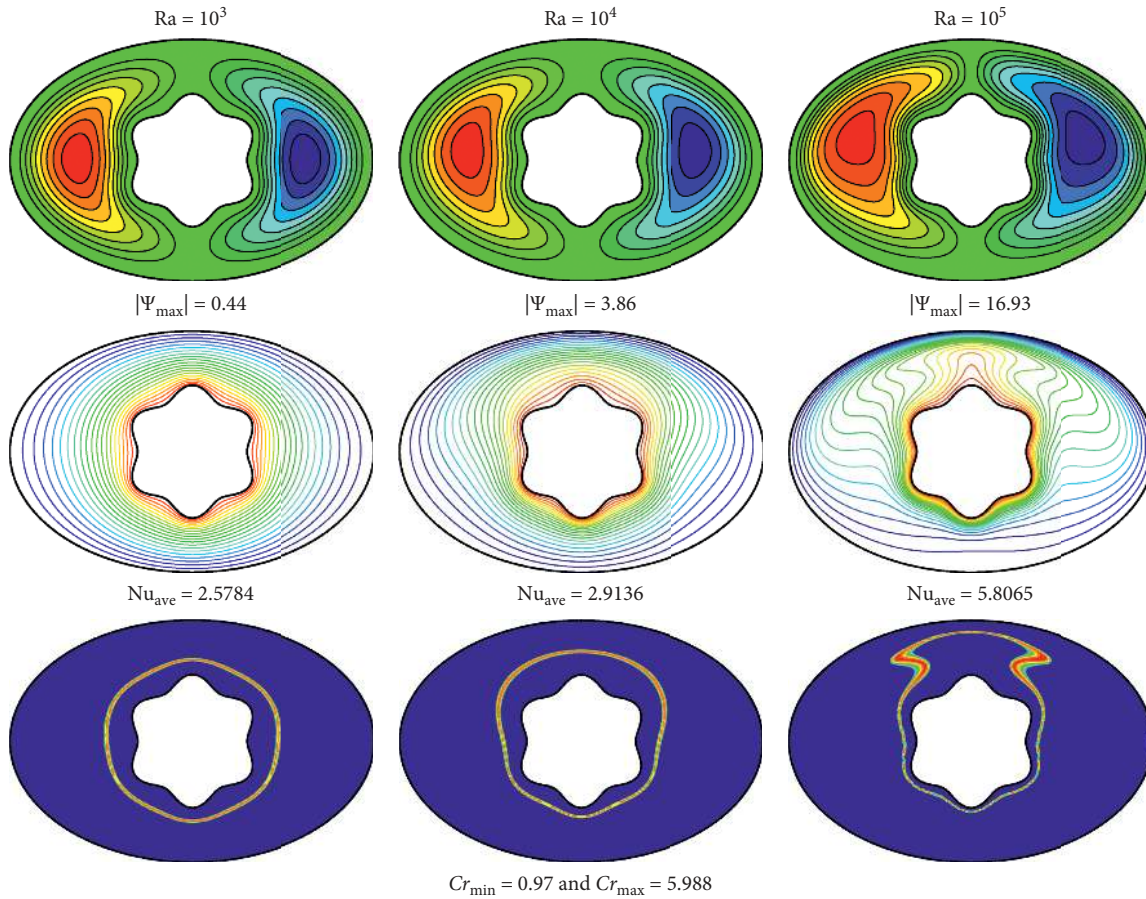| A	N	Ra	Ha	β	Da	Φ	Pr	θ_f	ϕ	λ	Ste	δ	Nc	Nv	Ns	ρ_p/ρ_f	$\phi \times \beta_p/\beta_f$
0.2	6	10^5	20	$30°$	10^{-2}	10^{-4}	6.2	0.5	0.05	0.4	0.313	0.05	3	3	1	0.9	0

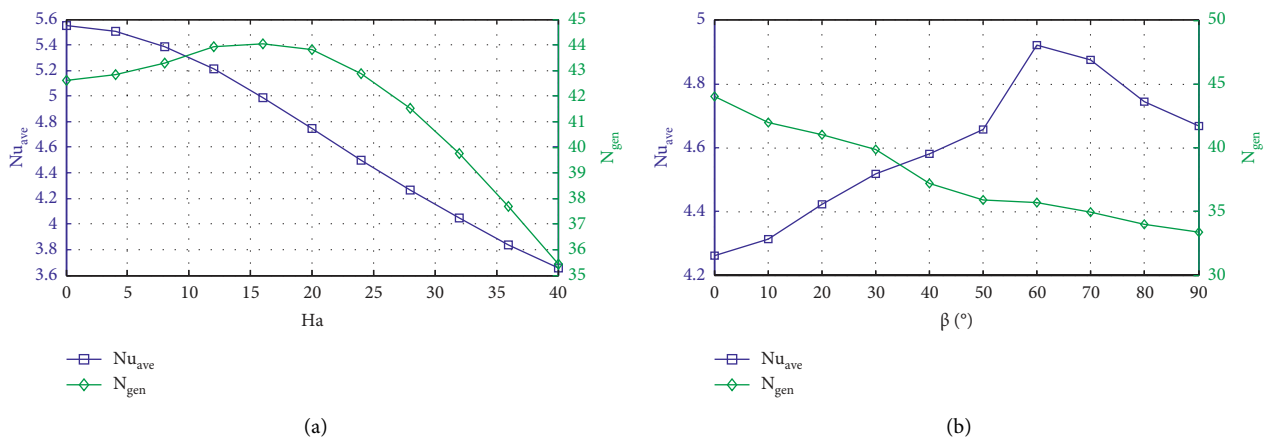FIGURE 3: The streamlines, the isotherms, and Cr contour at Ra $= 10^3$, 10^4, and 10^5.

(a)

(b)

FIGURE 4: The variations of Nu_{ave} and N_{gen} versus (a) the Hartmann number and (b) the angle of magnetic field.

(19.59% decreasing) when Ha increases from 16 to 40. This figure indicates that increasing the Hartmann number is desirable after Ha = 16. Figure 4(b) shows that Nu_{ave} firstly ascends, attains a maximum value, and then descends with ascending the angle of the magnetic field. The maximum value of Nu_{ave} is 4.9214, which occurs at $\beta = 60°$. On the other hand, N_{gen} decreases continuously from 44.03 to 33.36 (24.23% decreasing) when β increases from $0°$ to $90°$. Other decision parameters were assumed to be $\theta_f = 0.6$, $\beta = 0°$, $A = 0.1$, and $N = 8$ for Figure 4(a) while they are Ha = 10, Ste = 0.5, $\theta_f = 0.6$, $\phi = 0.04$, $A = 0.15$, and $N = 4$ without porosity for Figure 4(b).

Figure 5 presents variations of the entropy generation number and the average Nusselt number versus the fusion temperature of the NEPCM core (θ_f) at Ra = 10^5 and $\phi = 0.05$. It shows approximately a regular symmetrical behavior for $\theta_f = 0.5$ due to the symmetry of both the boundary conditions and geometry. The variations of the average Nusselt number are very small in the range of $0.3 < \theta_f < 0.65$, and there is a local minimum at $\theta_f = 0.5$. The maximum value of Nu_{ave} is 3.268 that occurs at $\theta_f = 0.4$ and $\theta_f = 0.6$. Besides, the entropy generation number firstly decreases to a minimum value and then goes up as the fusion temperature increases. The minimum value of N_{gen} is 39 that occurs at $\theta_f = 0.5$ although it is approximately constant in the range of $0.35 < \theta_f < 0.6$. This figure discovers that the best range of θ_f is $0.35 < \theta_f < 0.6$ from both second law analysis and heat transfer point of view. Other decision parameters were selected as Ha = 30, $\beta = 0°$, and $A = 0.3$.

Figure 6(a) demonstrates the variations of Nu_{ave} and N_{gen} versus Ste while the values of $|\Psi_{max}|$ and ECOP are calculated and plotted in Figure 6(b) as a function of Ste. It is obvious from the figure that Nu_{ave} decreases with ascending the values of Ste whilst the values of N_{gen} ascend as the values of Ste go up. Regarding the definition of the Stefan number (Ste), which is the ratio of the sensible heat to the latent heat of the PCM, the increasing Ste means descending the PCM core latent heat. The latter leads to a decrease in the heat storage capacity of the NEPCM particles, which concluded a lower rate of heat transfer. For instance, Nu_{ave} ascends from 4.6998 to 4.4673 (4.95% decreasing) while N_{gen} increases from 41.24 to 44.81 (8.65% increasing) when Ste increases from 0.2 to 0.7 at $\theta_f = 0.35$. Figure 6(b) illustrates that the values of $|\Psi_{max}|$ increase while the ECOP descends with ascending Ste. Therefore, the figure discovers that the heat transfer rate decreases although the fluid velocity enhances with increasing the Stefan number. Also, $|\Psi_{max}|$ increases 9.13% while the ECOP decreases 12.54% when Ste increases from 0.2 to 0.7. Other decision parameters for this figure are Ha = 22, $\beta = 0°$, $Nc = 6$, and $A = 0.15$.

Figure 7 represents the variations of Nu_{ave}, N_{gen}, $|\Psi_{max}|$, and ECOP versus ϕ. As shown, increasing ϕ is desirable since Nu_{ave} and ECOP raise and N_{gen} decreases with ascending ϕ. Albeit, the values of $|\Psi_{max}|$ decrease as ϕ increases. For example, Nu_{ave} increases from 5.4591 to 6.5446 (19.9% increasing) and ECOP ascends from 0.1273 to 0.1640 (28.8% amplified) while $|\Psi_{max}|$ decreases from 17.24 to 16.34 (5.2% decreasing) and N_{gen} decreases from 42.88 to 39.89 (6.9%
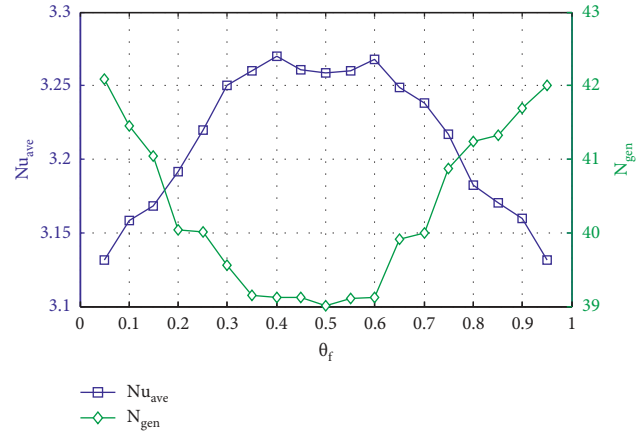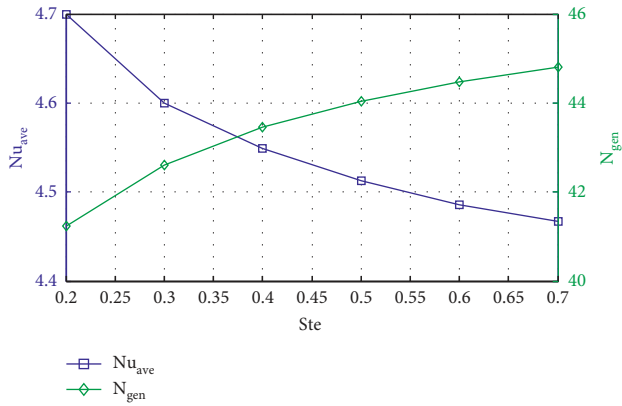

FIGURE 5: The variations of Nu_{ave} and N_{gen} versus the fusion temperature.

decreasing) when ϕ increases from 0 to 0.06. Regarding equation (6), decreasing the values of $|\Psi_{max}|$ is justifiable since the viscosity of nanofluid increases when the values of ϕ go up. Other decision parameters were assumed to be Ha = 18, $\beta = 60°$, $Nc = 6$, Da = 10, Ste = 0.2, $A = 0.1$, and $N = 5$.

Figure 8(a) presents variations of Nu_{ave} and N_{gen} versus the Darcy number while Figure 8(b) shows variations of $|\Psi_{max}|$ and ECOP against the Darcy number. From the figure, Nu_{ave}, $|\Psi_{max}|$, and ECOP ascend while the values of N_{gen} descend with ascending the Darcy number. For instance, Nu_{ave} increases from 6.0034 to 6.6509 (10.8% increasing), $|\Psi_{max}|$ increases from 15.42 to 19.46 (26.2% increasing), and ECOP ascends from 0.1270 to 0.1428 (12.4% amplified) while N_{gen} decreases from 47.26 to 46.57 (1.5% decreasing) when Darcy number ascends from 10^{-2} to 10^2 at $\theta_f = 0.45$. Other decision parameters are Ha = 10, $\beta = 35°$, $Nc = 6$, $A = 0.1$, and $N = 4$.

Figure 9 depicts the streamlines, the isotherms, and the Cr contours for different values of amplitude ($A = 0.1, 0.2,$ and 0.3). The streamlines follow the shape of the inner wall, especially near the hot wall. The flow velocity decreases with increasing the amplitude parameter as it can be understood from the values of $|\Psi_{max}|$. It can be due to this fact that the available space for fluid circulation decreases with increasing the values of A. The rate of heat transfer can be reflected by the shape of isotherms, where Nu_{ave} determines the value of it. The values of Nu_{ave} are 4.7929, 4.1158, and 3.4985 for $A = 0.1, 0.2,$ and 0.3, respectively. It is obvious from the figure that the values of Nu_{ave} descend with ascending the values of A. Here, it can be stated that increasing the A values is similar to increasing the Ra values. Also, it should be noticed that the values of N_{gen} are 41.01, 40.86, and 40.31 for $A = 0.1, 0.2,$ and 0.3, respectively. Therefore, increasing the values of amplitude is desirable from the second law of thermodynamics viewpoint. The last row of this figure demonstrates the Cr contours where the phase change region is specified by the color region. The value of Cr is 0.964 (outside the fusion region corresponding to $\phi = 0.06$) while it changes inside the fusion region where it has a maximum value of 10.389
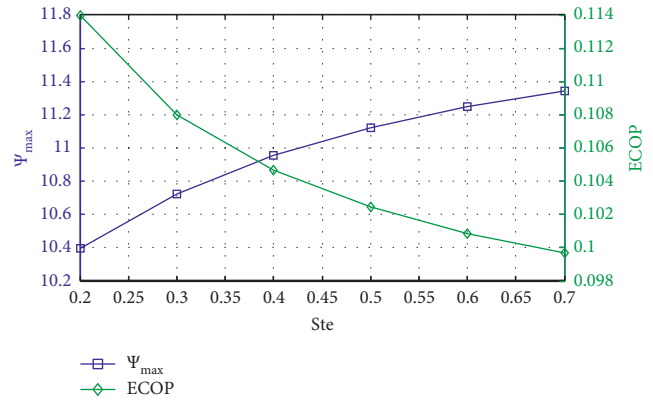
FIGURE 6: (a) The variations of Nu_{ave} and N_{gen} versus Stefan number and (b) the variations of $|\psi_{\text{max}}|$ and ECOP versus Stefan number.
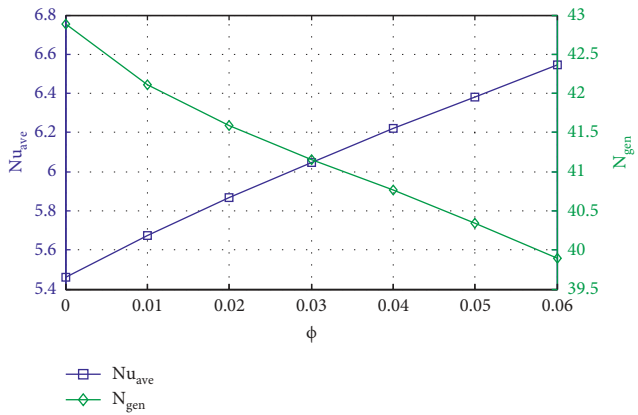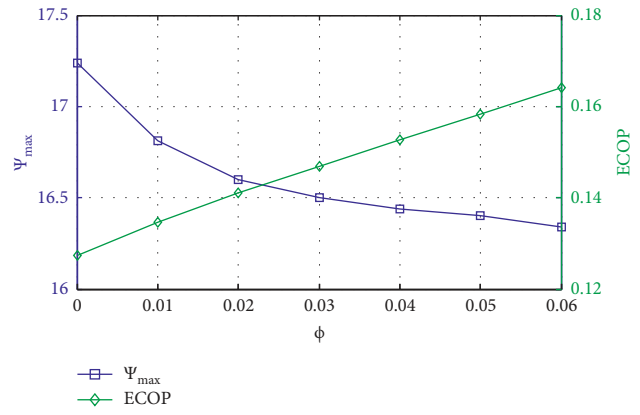
FIGURE 7: (a) The variations of Nu_{ave} and N_{gen} versus volume fraction of nanoparticles and (b) the variations of $|\psi_{\text{max}}|$ and ECOP versus volume fraction of nanoparticles.
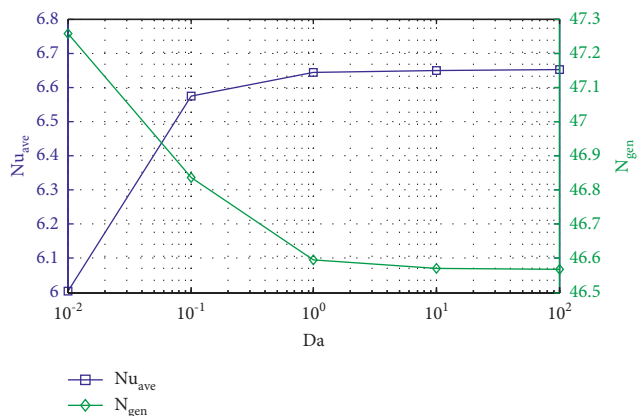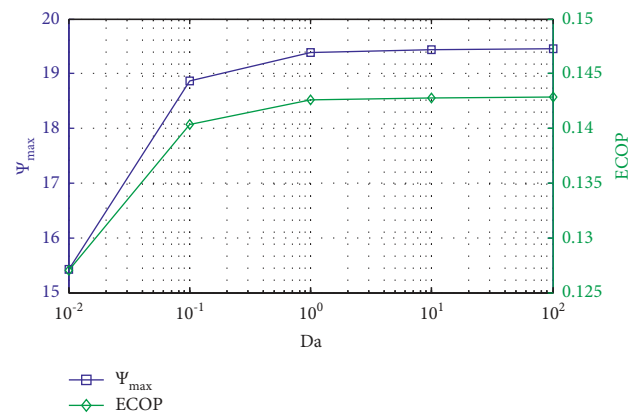

FIGURE 8: (a) The variations of Nu_{ave} and N_{gen} versus Darcy number and (b) the variations of $|\psi_{\text{max}}|$ and ECOP versus Darcy number.

$A = 0.1$ $A = 0.2$ $A = 0.3$

$|\Psi_{\text{max}}| = 10.14$ $|\Psi_{\text{max}}| = 10.07$ $|\Psi_{\text{max}}| = 9.92$

$Nu_{\text{ave}} = 4.7929$ $Nu_{\text{ave}} = 4.1158$ $Nu_{\text{ave}} = 3.4985$
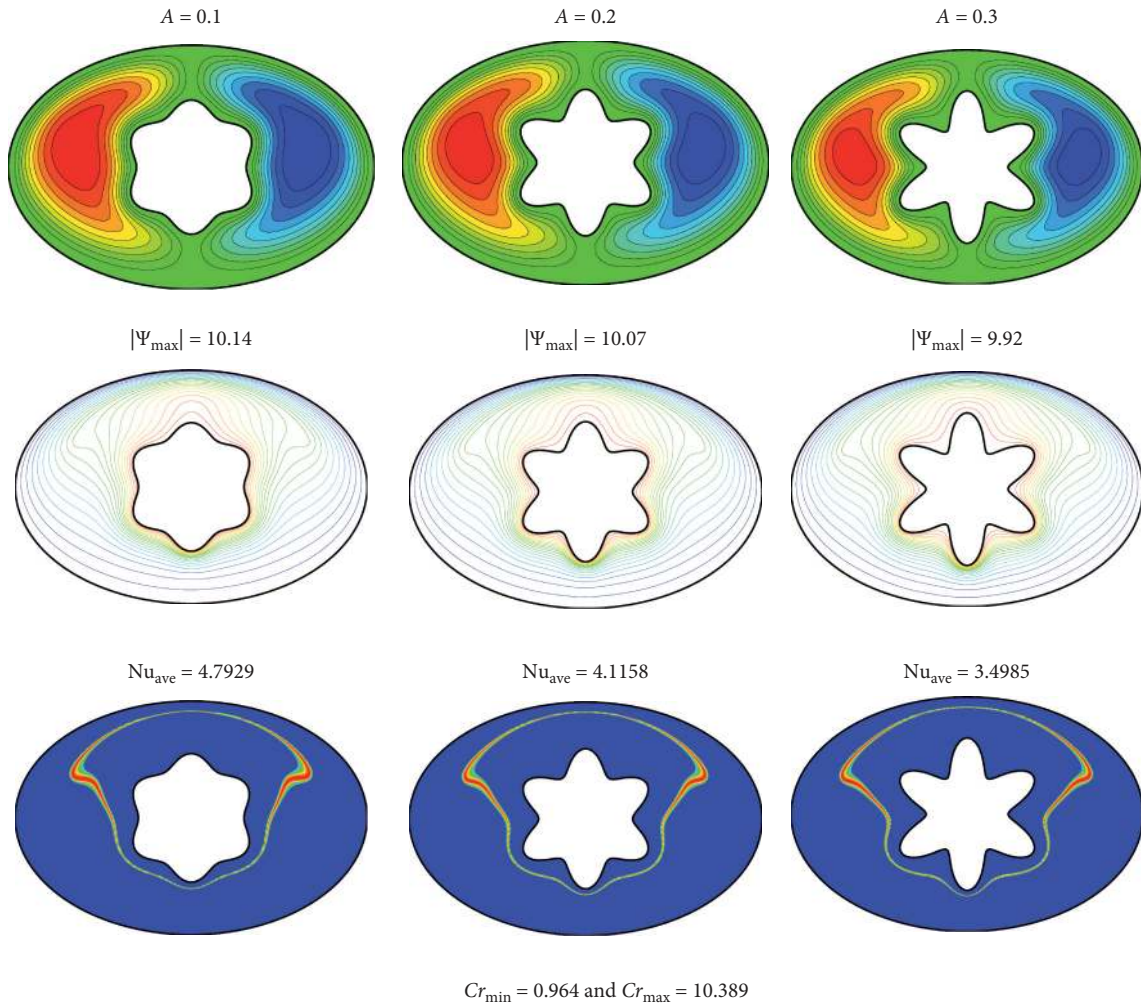
$Cr_{\text{min}} = 0.964$ and $Cr_{\text{max}} = 10.389$

FIGURE 9: The streamlines, the isotherms, and Cr contour at $A = 0.1$, 0.2, and 0.3.

in this figure for each value of the amplitude parameter. The Cr contour is similar to a plume for each value of A. In this figure, a horizontal magnetic field $(\text{Ha} = 25, \beta = 0°)$ has been considered.

Figure 10 illustrates the streamlines, the isotherms, and the Cr contours for the various numbers of undulation $(N = 4, 5, \text{and } 6)$. As shown by the figure, the values of $|\Psi_{\text{max}}|$ are 12.83, 12, 65, and 12.21 that indicate the velocity of fluid flow decreases slightly as the values of N increase. The reason could be an increase in the number of obstacles in the path. The red lines in the isotherms show higher temperatures that move from the wavy wall to the enclosure wall. The values of Nu_{ave} are 5.0886, 4.6966, and 4.4593 for $N = 4, 5, \text{and } 6$, respectively. So, the value of Nu_{ave} decreases 12.4% when ascends from 4 to 6. The values of N_{gen} are 44.07, 43.46, and 44.80 for $N = 4, 5, \text{and } 6$, respectively. Thus, a minimum value can be seen for N_{gen} at $N = 5$. As shown by the Cr contours, the width of the ribbon shape is not the same everywhere. The ribbon shape is wider where the temperature gradients are smooth. Here, we have $Cr_{\text{min}} = 0.976$ and $Cr_{\text{max}} = 7.2592$ for $\phi = 0.04$. Other decision parameters are $\text{Ha} = 18$, $\beta = 0°$, and $\text{Ste} = 2$.

Figures 11(a)–11(d) present the contribution of the heat transfer $(N_{T,\text{HT}})$, the fluid friction $(N_{T,\text{FF}})$, and the magnetic field $(N_{T,\text{MF}})$ in the total entropy generation number for an enclosure without porous medium. Comparison between Figures (a) and (b) discovers that $N_{T,\text{FF}}$ increases from 10% to 43% while $N_{T,\text{HT}}$ decreases from 74% to 15% as the Rayleigh number attains from 10^4 to 10^5. Its reason is increasing fluid flow velocity (ascending the values of $|\Psi_{\text{max}}|$) with ascending the Rayleigh number. As we know, the friction losses enhance with enhancement of fluid flow velocity. Also, a comparison between Figures (c) and (d) indicates that $N_{T,\text{HT}}$ ascends from 15% to 19% as ϕ ascends from 0.01 to 0.06. Regarding the first term in the right-hand side of equation (12), increasing of $N_{T,\text{HT}}$ is justifiable. Figures 11(e)–11(h) show the contribution of the heat transfer $(N_{T,\text{HT}})$, the fluid friction $(N_{T,\text{FF}})$, the magnetic field $(N_{T,\text{MF}})$, and the porous medium $(N_{T,\text{PM}})$ in N_{gen}. Comparison between Figures (e) and (f) reveals that $N_{T,\text{MF}}$ increases from 22% to 49% while other type of irreversibilities decreases when the Hartmann number increases from 12 to 24. The value of $N_{T,\text{MF}}$ increases with ascending Ha as shown by the last term in equation (12).

$N = 4$ $N = 5$ $N = 6$

$|\Psi_{max}| = 12.83$ $|\Psi_{max}| = 12.65$ $|\Psi_{max}| = 12.21$

$Nu_{ave} = 5.0886$ $Nu_{ave} = 4.6966$ $Nu_{ave} = 4.4593$

$Cr_{min} = 0.976$ and $Cr_{max} = 7.2592$
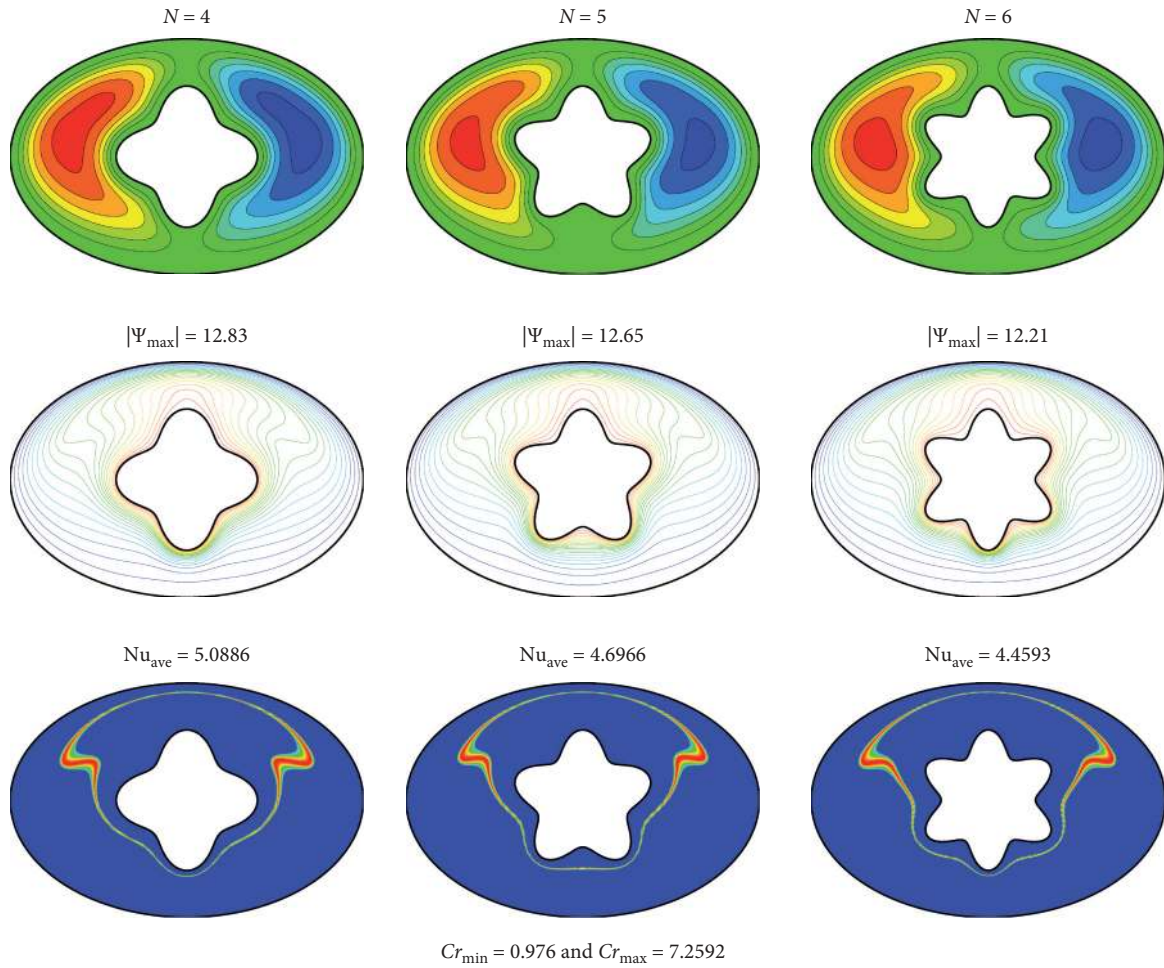
FIGURE 10: The streamlines, the isotherms, and Cr contour at $N = 4, 5,$ and 6.

(a): Ra = 10^4 (b): Ra = 10^5 (e): Ha = 12   (f): Ha = 24

(c): ϕ = 0.01   (d): ϕ = 0.06   (g): Ste = 0.2   (h): Ste = 0.5

$N_{T,HT}$
$N_{T,FF}$
$N_{T,MF}$

$N_{T,HT}$ $N_{T,MF}$
$N_{T,FF}$ $N_{T,PM}$

(a)   (b)

FIGURE 11: Contribution of components in N_{gen} for different values of Ra, ϕ, Ha, and Ste.

5. Conclusion

The entropy generation and heat transfer analysis were investigated in a complex cavity filled with NEPCMs suspension. The nondimensional governing equations were solved by CVFEM. Here, significant outcomes are remembered as follows:
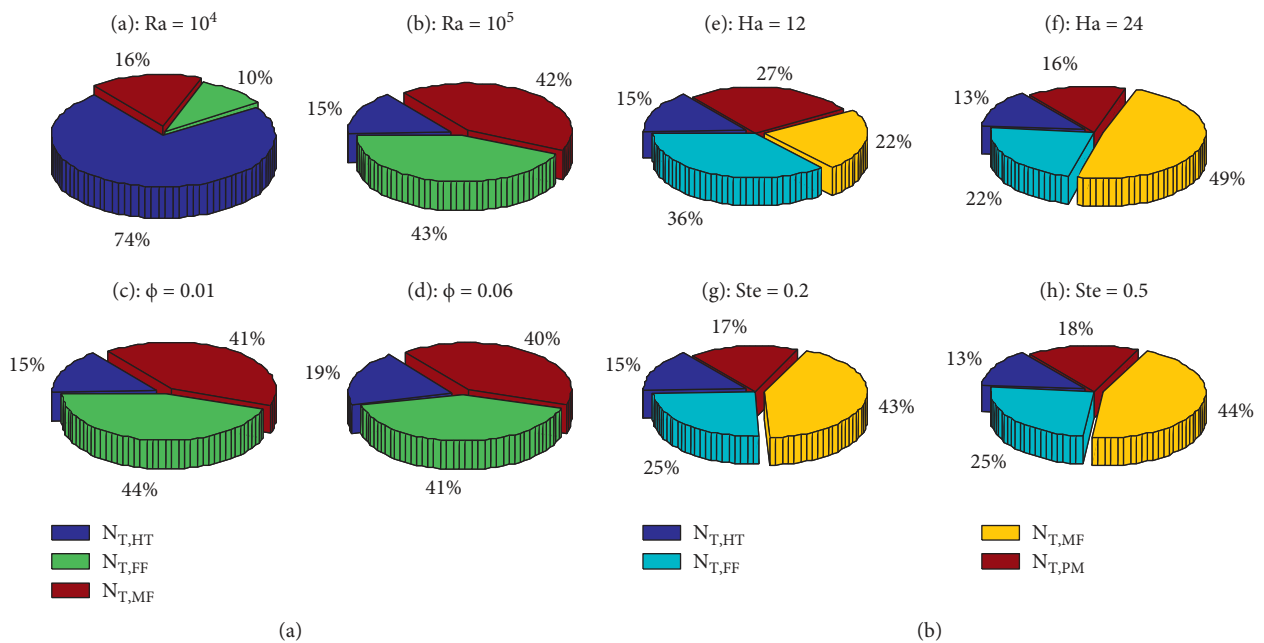
(i) The values of $|\Psi_{max}|$, Nu_{ave}, and N_{gen} rise with ascending Ra. The values of $|\Psi_{max}|$ are 0.44, 3.86, and 16.93, the values of Nu_{ave} are 2.5784, 2.9136, and 5.8065, and the values of N_{gen} are 3.03, 4.61, and 45.91, for Ra = 10^4, 10^5, and 10^6, respectively (Figure 3). These values indicate that fluid velocity and rate of heat transfer increase with increasing the Rayleigh number.

(ii) The values of Nu_{ave} descend with ascending Ha while N_{gen} has a maximum at Ha = 16. Also, there is a maximum value for Nu_{ave} at $\beta = 60°$ (Figure 4).

(iii) Symmetrical behavior was seen for Nu_{ave} and N_{gen} with respect to $\theta_f = 0.5$. The maximum value of Nu_{ave} is 3.268 that occurs at $\theta_f = 0.4$ and $\theta_f = 0.6$ while there is a minimum value for N_{gen} that equals 39 and happens at $\theta_f = 0.5$ (Figure 5).

(iv) Lower values of Ste are desirable because Nu_{ave} descends and N_{gen} ascends with Ste (Figure 6). Indeed, as the latent heat of the PCM cores rises, the Stefan number decreases.

(v) Nu_{ave} increases 19.9%, and ECOP increases 28.8% while N_{gen} decreases by 6.9% when ϕ enhances from 0 to 0.06 (Figure 7).

(vi) Higher values of Da are suitable since the values of ECOP and Nu_{ave} increase while N_{gen} descends with ascending Da (Figure 8). It must be recalled that the ECOP represents the performance of the cavity.

(vii) The effects of A and N on the streamlines, the isotherms, and the Cr contours show that lower values of these parameters are proper (Figures 9 and 10).

(viii) The contribution of $N_{T,MF}$ ascends from 22% to 49% as Ha goes up from 12 to 24. Also, the value of $N_{T,FF}$ increases while the value of $N_{T,HT}$ descends with ascending Ra (Figures 11).

Nomenclature

A: Amplitude
B_0: Magnetic field strength (T)
C_p: Specific heat at constant pressure (J kg^{-1} K^{-1})
Cr: The heat capacity ratio defined by equation (7)
f: The nondimensional fusion function defined by equation (8)
Da: Darcy number
ECOP: Ecological coefficient of performance
g: Gravitational acceleration (ms^{-2})
Ha: Hartmann number
k: Thermal conductivity (Wm^{-1}K^{-1})
K: Permeability of the medium (m^2)
L: Gap between the inner and outer walls of the enclosure (m)
N: Number of undulations
N_{gen}: Entropy generation number
Nc: Thermal conductivity parameter
Ns: Electrical conductivity parameter
Nu: Nusselt number
Nv: Viscosity parameter
Pr: Prandtl number
Ra: Rayleigh number
Ste: Stefan number
$\dot{S}_{gen}$: Rate of entropy generation per unit volume (J s^{-1} K^{-1} m^{-3})
T: Temperature (K)
T_0: Mean temperature (K) $(T_0 = (T_h + T_c)/2)$
u, v: Components of velocity (m s^{-1})
X, Y: Dimensionless coordinates

Greek Letters

α: Thermal diffusivity (m^{2}s^{-1})
β: Angle of magnetic field (°)
β_T: Thermal expansion coefficient (K^{-1})
δ: Nondimensional parameter of fusion range
Θ: Dimensionless temperature
ζ: Rotation angle (°)
λ: Ratio of the heat capacity of the NEPCM nanoparticles to the base fluid
μ: Dynamic viscosity (N s m^{-2})
v: Kinematic viscosity (m^{2}s^{-1})
ρ: Density (kg m^{-3})
σ: Electrical conductivity (Ω/m)
ΔT: Temperature difference (K) $(\Delta T = T_h - T_c)$
ϕ: Volume fraction of NEPCM nanoparticles
Φ: Irreversibility distribution ratio $(\Phi_f = (\mu_f T_0/k_f)(\alpha_f/L\Delta T)^2)$
Ψ: Dimensionless stream function
Ω: Dimensionless vorticity

Subscripts

ave: Average
b: Bulk properties of the suspension
c: Cold
f: Fluid
FF: Fluid friction
gen: Generation
h: Hot
HT: Heat transfer
L: Local
max: Maximum
MF: Magnetic field
PM: Porous medium
s: Solid.

Data Availability

The data used to support this study are available from the corresponding author upon request.

Conflicts of Interest

The authors declare that they have no conflicts of interest.

References

[1] M. H. Ahmadi, M. Sadeghzadeh, H. Maddah, A. Solouk, R. Kumar, and K.-W. Chau, "Precise smart model for estimating dynamic viscosity of SiO2/ethylene glycol-water nanofluid," *Engineering Applications of Computational Fluid Mechanics*, vol. 13, no. 1, pp. 1095–1105, 2019.

[2] S. M. Seyyedi, A. S. Dogonchi, M. Hashemi-Tilehnoee, Z. Asghar, M. Waqas, and D. D. Ganji, "A computational framework for natural convective hydromagnetic flow via inclined cavity: an analysis subjected to entropy generation," *Journal of Molecular Liquids*, vol. 287, Article ID 110863, 2019.

[3] A. S. Dogonchi, M. Waqas, S. R. Afshar et al., "Investigation of magneto-hydrodynamic fluid squeezed between two parallel disks by considering Joule heating, thermal radiation, and adding different nanoparticles," *International Journal of Numerical Methods for Heat and Fluid Flow*, vol. 30, no. 2, pp. 659–680, 2020.

[4] M. Jamei, I. Ahmadianfar, I. A. Olumegbon et al., "On the specific heat capacity estimation of metal oxide-based nanofluid for energy perspective—a comprehensive assessment of data analysis techniques," *International Communications in Heat and Mass Transfer*, vol. 123, Article ID 105217, 2021.

[5] I. Zahmatkesh, M. Sheremet, L. Yang et al., "Effect of nanoparticle shape on the performance of thermal systems utilizing nanofluids: a critical review," *Journal of Molecular Liquids*, vol. 321, Article ID 114430, 2020.

[6] S. O. Giwa, M. Sharifpur, J. P. Meyer, S. Wongwises, and O. Mahian, "Experimental measurement of viscosity and electrical conductivity of water-based γ-Al2O3/MWCNT hybrid nanofluids with various particle mass ratios," *Journal of Thermal Analysis and Calorimetry*, vol. 143, no. 2, pp. 1037–1050, 2021.

[7] M. Hashemi-Tilehnoee, A. S. Dogonchi, S. M. Seyyedi, A. J. Chamkha, and D. D. Ganji, "Magnetohydrodynamic natural convection and entropy generation analyses inside a nanofluid filled incinerator-shaped porous cavity with wavy heater block," *Journal of Thermal Analysis and Calorimetry*, vol. 1, pp. 1–13, 2020.

[8] M. Mahdavi, M. Sharifpur, M. H. Ahmadi, and J. P. Meyer, "Nanofluid flow and shear layers between two parallel plates: a simulation approach," *Engineering Applications of Computational Fluid Mechanics*, vol. 14, no. 1, pp. 1536–1545, 2020.

[9] S. Mondal, A. S. Dogonchi, N. Tripathi et al., "A theoretical nanofluid analysis exhibiting hydromagnetics characteristics employing CVFEM," *Journal of the Brazilian Society of Mechanical Sciences and Engineering*, vol. 42, no. 1, pp. 1–12, 2020.

[10] S. O. Giwa, M. Sharifpur, M. H. Ahmadi, and J. P. Meyer, "A review of magnetic field influence on natural convection heat transfer performance of nanofluids in square cavities," *Journal of Thermal Analysis and Calorimetry*, vol. 145, pp. 2581–2623, 2021.

[11] M. Mahdavi, M. Sharifpur, M. H. Ahmadi, and J. P. Meyer, "Aggregation study of Brownian nanoparticles in convective phenomena," *Journal of Thermal Analysis and Calorimetry*, vol. 135, no. 1, pp. 111–121, 2019.

[12] M. Hashemi-Tilehnoee, S. Tashakor, A. S. Dogonchi, S. M. Seyyedi, and M. Khaleghi, "Entropy generation in concentric annuli of 400 kV gas-insulated transmission line," *Thermal Science and Engineering Progress*, vol. 19, p. 100614, 2020.

[13] S. M. Seyyedi, A. S. Dogonchi, M. Hashemi-Tilehnoee, M. Waqas, and D. D. Ganji, "Entropy generation and economic analyses in a nanofluid filled L-shaped enclosure subjected to an oriented magnetic field fluid filled L-shaped enclosure subjected to an oriented magnetic field," *Applied Thermal Engineering*, vol. 168, p. 114789, 2020.

[14] S. M. Seyyedi, A. S. Dogonchi, M. Hashemi-Tilehnoee, D. D. Ganji, and A. J. Chamkha, "Second law analysis of magneto-natural convection in a nanofluid filled wavy-hexagonal porous enclosurefluid filled wavy-hexagonal porous enclosure," *International Journal of Numerical Methods for Heat and Fluid Flow*, vol. 30, no. 11, pp. 4811–4836, 2020.

[15] H. Cui, W. Tang, Q. Qin, F. Xing, W. Liao, and H. Wen, "Development of structural-functional integrated energy storage concrete with innovative macro-encapsulated PCM by hollow steel ball," *Applied Energy*, vol. 185, pp. 107–118, 2017.

[16] Y.-C. Weng, H.-P. Cho, C.-C. Chang, and S.-L. Chen, "Heat pipe with PCM for electronic cooling," *Applied Energy*, vol. 88, no. 5, pp. 1825–1833, 2011.

[17] L. Miró, J. Gasia, and L. F. Cabeza, "Thermal energy storage (TES) for industrial waste heat (IWH) recovery: a review," *Applied Energy*, vol. 179, pp. 284–301, 2016.

[18] A. El-Sawi, F. Haghighat, and H. Akbari, "Assessing long-term performance of centralized thermal energy storage system," *Applied Thermal Engineering*, vol. 62, no. 2, pp. 313–321, 2014.

[19] V. Palomba, V. Brancato, and A. Frazzica, "Experimental investigation of a latent heat storage for solar cooling applications," *Applied Energy*, vol. 199, pp. 347–358, 2017.

[20] A. H. Mosaffa, F. Talati, M. A. Rosen, and H. B. Tabrizi, "Approximate analytical model for PCM solidification in a rectangular finned container with convective cooling boundariesfication in a rectangular finned container with convective cooling boundaries," *International Communications in Heat and Mass Transfer*, vol. 39, no. 2, pp. 318–324, 2012.

[21] M. Taghilou and F. Talati, "Numerical investigation on the natural convection effects in the melting process of PCM in a finned container using lattice Boltzmann method finned container using lattice Boltzmann method," *International Journal of Refrigeration*, vol. 70, pp. 157–170, 2016.

[22] V. Kumaresan, R. Velraj, and S. K. Das, "The effect of carbon nanotubes in enhancing the thermal transport properties of PCM during solidificationfication," *Heat and Mass Transfer*, vol. 48, no. 8, pp. 1345–1355, 2012.

[23] A. H. Mosaffa, C. A. Infante Ferreira, F. Talati, and M. A. Rosen, "Thermal performance of a multiple PCM thermal storage unit for free cooling," *Energy Conversion and Management*, vol. 67, pp. 1–7, 2013.

[24] A. M. Sojoudi, A. FiSaha, M. Cholette, S. C. Saha, and M. Cholette, "Multi-layer PCM solidification in a finned triplex tube considering natural convectionfication in a finned triplex tube considering natural convection," *Applied Thermal Engineering*, vol. 123, pp. 901–916, 2017.

[25] X. Huang, C. Zhu, Y. Lin, and G. Fang, "Thermal properties and applications of microencapsulated PCM for thermal energy storage: a review," *Applied Thermal Engineering*, vol. 147, pp. 841–855, 2019.

[26] M. A. Hamdan and I. Al-Hinti, "Analysis of heat transfer during the melting of a phase-change material," *Applied Thermal Engineering*, vol. 24, no. 13, pp. 1935–1944, 2004.

[27] M. Azad, D. Dineshan, D. Groulx, and D. Adam, "Melting of phase change materials in a cylindrical enclosure: parameters influencing natural convection onset," in *Proceedings of the 4th International Forum on Heat Transfer, IFHT 2016*, Sendai, Japan, November 2016.

[28] A. Vikas and S. K. Soni, "Simulation of melting process of a phase change material (PCM) using ANSYS (fluent)," *International Research Journal of Engineering and Technology (IRJET)*, vol. 4, no. 5, 2017.

[29] F. Souayfane, P. H. Biwole, and F. Fardoun, "Melting of a phase change material in presence of natural convection and radiation: a simplified model," *Applied Thermal Engineering*, vol. 130, pp. 660–671, 2017.

[30] F. Selimefendigil, H. F. Oztop, and A. J. Chamkha, "Natural convection in a CuO–water nanofluid filled cavity under the effect of an inclined magnetic field and phase change material (PCM) attached to its vertical wall," *Journal of Thermal Analysis and Calorimetry*, vol. 135, no. 2, 2019.

[31] M. J. Hosseini, A. A. Ranjbar, K. Sedighi, and M. Rahimi, "A combined experimental and computational study on the melting behavior of a medium temperature phase change storage material inside shell and tube heat exchanger," *International Communications in Heat and Mass Transfer*, vol. 39, no. 9, pp. 1416–1424, 2012.

[32] M. J. Hosseini, M. Rahimi, and R. Bahrampoury, "Experimental and computational evolution of a shell and tube heat exchanger as a PCM thermal storage system," *International Communications in Heat and Mass Transfer*, vol. 50, pp. 128–136, 2014.

[33] S.. Seddegh, M. M. Joybari, X. Wang, and F. Haghighat, "Experimental and numerical characterization of natural convection in a vertical shell-and-tube latent thermal energy storage system," *Sustainable Cities and Society*, vol. 35, 2017.

[34] I. Jmal and M. Baccar, "Numerical investigation of PCM solidification in a finned rectangular heat exchanger including natural convection fication in a finned rectangular heat exchanger including natural convection," *International Journal of Heat and Mass Transfer*, vol. 127, pp. 714–727, 2018.

[35] M. Ghalambaz, A. J. Chamkha, and D. Wen, "Natural convective flow and heat transfer of Nano-Encapsulated Phase Change Materials (NEPCMs) in a cavity," *International Journal of Heat and Mass Transfer*, vol. 138, pp. 738–749, 2019.

[36] H. Ahmad, S. A. Mehryan, and M. Ghalambaz, "Time periodic natural convection heat transfer in a nano-encapsulated phase-change suspension," *International Journal of Mechanical Sciences*, vol. 166, 2019.

[37] M. Hashemi-Tilehnoee, A. S. Dogonchi, S. M. Seyyedi, and M. Sharifpur, "Magneto-fluid dynamic and second law analysis in a hot porous cavity filled by nanofluid and nano-encapsulated phase change material suspension with different layout of cooling channels," *Journal of Energy Storage*, vol. 31, Article ID 101720, 2020.

[38] G. Nagaraju, J. Srinivas, J. V. Ramana Murthy, and A. M. Rashad, "Entropy generation analysis of the MHD flow of couple stress fluid between two concentric rotating cylinders with porous lining," *Heat Transfer—Asian Research*, vol. 46, no. 4, 2017.

[39] A. M. Rashad, T. Armaghani, A. J. Chamkha, and M. A. Mansour, "Entropy generation and MHD natural convection of a nanofluid in an inclined square porous cavity: effects of a heat sink and source size and location," *Chinese Journal of Physics*, vol. 56, no. 1, pp. 193–211, 2018.

[40] T. Armaghani, C. Ali, A. M. Rashad, and M. A. Mansour, "Inclined magneto: convection, internal heat, and entropy generation of nanofluid in an I-shaped cavity saturated with porous media," *Journal of Thermal Analysis and Calorimetry*, vol. 142, pp. 2273–2285, 2020.

[41] M. A. Siddiqui, A. Riaz, I. Khan, and K. S. Nisar, "Augmentation of mixed convection heat transfer in a lid-assisted square enclosure utilizing micropolar fluid under magnetic environment: a numerical approach," *Results in Physics*, vol. 18, Article ID 103245, 2020.

[42] M. K. Nayak, A. S. Dogonchi, Y. Elmasry, N. Karimi, A. J. Chamkha, and H. Alhumade, "Free convection and second law scrutiny of NEPCM suspension inside a wavy-baffle-equipped cylinder under altered Fourier theory," *Journal of the Taiwan Institute of Chemical Engineers*, 2021.

[43] A. S. Dogonchi, M. Waqas, S. M. Seyyedi, M. Hashemi-Tilehnoee, and D. D. Ganji, "CVFEM analysis for Fe3O4-H2O nanofluid in an annulus subject to thermal radiation fluid in an annulus subject to thermal radiation," *International Journal of Heat and Mass Transfer*, vol. 132, pp. 473–483, 2019.

[44] A. S. Dogonchi, M. Waqas, and D. D. Ganji, "Shape effects of Copper-Oxide (CuO) nanoparticles to determine the heat transfer filled in a partially heated rhombus enclosure: CVFEM approach filled in a partially heated rhombus enclosure: CVFEM approach," *International Communications in Heat and Mass Transfer*, vol. 107, pp. 14–23, 2019.

[45] I. Tlili, S. M. Seyyedi, S. M. Seyyedi, A. S. Dogonchi, M. Hashemi-Tilehnoee, and D. D. Ganji, "Analysis of a single-phase natural circulation loop with hybrid-nanofluid," *International Communications in Heat and Mass Transfer*, vol. 112, p. 104498, 2020.

[46] A. Sattar Dogonchi, T. Tayebi, N. Karimi, A. J. Chamkha, and H. Alhumade, "Thermal-natural convection and entropy production behavior of hybrid nanoliquid flow under the effects of magnetic field through a porous wavy cavity embodies three circular cylinders," *Journal of the Taiwan Institute of Chemical Engineers*, vol. 124, pp. 1–12, 2021.

[47] S. M. Seyyedi, "On the entropy generation for a porous enclosure subject to a magnetic field: different orientations of cardioid geometry," *International Communications in Heat and Mass Transfer*, vol. 116, Article ID 104712, 2020.

[48] A. S. Dogonchi, Z. Asghar, and M. Waqas, "CVFEM simulation for FeO-HO nanofluid in an annulus between two triangular enclosures subjected to magnetic field and thermal radiation," *International Communications in Heat and Mass Transfer*, vol. 112, Article ID 104449, 2020.

[49] M. M. Bhatti, A. Riaz, L. Zhang, S. M Sait, and R. Ellahi, "Biologically inspired thermal transport on the rheology of Williamson hydromagnetic nanofluid flow with convection: an entropy analysis," *Journal of Thermal Analysis and Calorimetry*, vol. 144, no. 6, pp. 2187–2202, 2021.

[50] A. Riaz, M. M. Bhatti, R. Ellahi, A. Zeeshan, and M. Sait, "Mathematical analysis on an asymmetrical wavy motion of blood under the influence entropy generation with convective boundary conditions fluence entropy generation with convective boundary conditions," *Symmetry*, vol. 12, no. 1, p. 102, 2020.

[51] A. Riaz, R. Ellahi, S. M Sait, and T. Muhammad, "Magnetized Jeffrey nanofluid with energy loss in between an annular part of two micro nonconcentric pipes," *Energy Sources, Part A: Recovery, Utilization, and Environmental Effects*, 2020.

[52] E. L. Alisetti and S. K. Roy, "Forced convection heat transfer to phase change material slurries in circular ducts," *Journal of Thermophysics and Heat Transfer*, vol. 14, no. 1, pp. 115–118, 2000.

[53] S. M. Seyyedi, A. S. Dogonchi, D. D. Ganji, and M. Hashemi-Tilehnoee, "Entropy generation in a nanofluid-filled semi-annulus cavity by considering the shape of nanoparticles," *Journal of Thermal Analysis and Calorimetry*, vol. 138, no. 2, pp. 1607–1621, 2019.